inorganics

MDPI

Article

High-Temperature Wide Thermal Hysteresis of an Iron(II) Dinuclear Double Helicate

Shiori Hora [1] and Hiroaki Hagiwara [2,*]

[1] Graduate School of Education, Gifu University, Yanagido 1-1, Gifu 501-1193, Japan; v1131032@edu.gifu-u.ac.jp

[2] Department of Chemistry, Faculty of Education, Gifu University, Yanagido 1-1, Gifu 501-1193, Japan

* Correspondence: hagiwara@gifu-u.ac.jp; Tel.: +81-58-293-2253

Received: 28 June 2017; Accepted: 25 July 2017; Published: 28 July 2017

Abstract: Two new dinuclear iron(II) complexes (**1·PF$_6$** and **1·AsF$_6$**) of the general formula $[Fe^{II}_2(L2^{C3})_2](X)_4{\cdot}nH_2O{\cdot}mMeCN$ (X = PF_6, n = m = 1.5 for **1·PF$_6$** and X = AsF_6, n = 3, m = 1 for **1·AsF$_6$**) have been prepared and structurally characterized, where $L2^{C3}$ is a bis-1,2,3-triazolimine type Schiff-base ligand, 1,1′-[propane-1,3-diylbis(1*H*-1,2,3-triazole-1,4-diyl)]bis{*N*-[2-(pyridin-2-yl)ethyl]methanimine}. Single crystal X-ray structure analyses revealed that **1·PF$_6$** and **1·AsF$_6$** are isostructural. The complex-cation $[Fe^{II}_2(L2^{C3})_2]^{4+}$ of both has the same dinuclear double helicate architecture, in which each iron(II) center has an N6 octahedral coordination environment. Neighboring helicates are connected by intermolecular π–π interactions to give a chiral one-dimensional (1D) structure, and cationic 1D chains with the opposite chirality exist in the crystal lattice to give a heterochiral crystal. Magnetic and differential scanning calorimetry (DSC) studies were performed only for **1·AsF$_6$**, since the thermal stability in a high-temperature spin crossover (SCO) region of **1·PF$_6$** is poorer than that of **1·AsF$_6$**. **1·AsF$_6$** shows an unsymmetrical hysteretic SCO between the low-spin–low-spin (LS–LS) and high-spin–high-spin (HS–HS) states at above room temperature. The critical temperatures of warming (T_c↑) and cooling (T_c↓) modes in the abrupt spin transition area are 485 and 401 K, respectively, indicating the occurrence of 84 K-wide thermal hysteresis in the first thermal cycle.

Keywords: double helicate; hysteresis; spin crossover; iron; 1,2,3-triazolimine; π–π interaction

1. Introduction

The interconversion between a high-spin (HS) and a low-spin (LS) state, the so-called "spin crossover" (SCO), is one of the most attractive phenomena in the field of molecular bistability [1–3]. This phenomenon is observed in $3d^4$–$3d^7$ transition metal complexes with various coordination geometries (e.g., octahedral, square-pyramidal, trigonal-bipyramidal, tetrahedral, etc.) [1,4–7], and is triggered by an external stimulus such as temperature, pressure, light irradiation, or a magnetic field [1–3]. While SCO originates from an individual metal center, a spin transition profile, for example, abruptness and multi-steps with or without hysteresis, is provided from the cooperative effect between SCO metal sites through intra- or intermolecular pathways [1–3]. There is a need for SCO materials which are capable of abrupt and complete HS–LS interconversion at around room temperature (RT) with wide thermal hysteresis width (ΔT) for potential applications in molecular memories, switches, and display devices. As such, various cooperative SCO compounds have been produced with supramolecular assembly via intermolecular hydrogen bonding [8–10] and π–π stacking [11–13], or coordination polymeric architecture by using bridging ligands [14–18]. Multinuclear clusters have also been widely studied in the hope of developing multistable compounds with more accessible spin states towards denser information storage, or hybrid SCO materials with multifunctional properties (e.g., SCO with charge transfer, magnetic coupling, luminescence, etc.) arising from the combination of the SCO metal center and other metal centers [2,19–24]. In particular, dinuclear species have received

much attention since they are a simple model for revealing intra- and intermolecular interactions for enhancing cooperativity [25–34]. From a more practical point of view, the importance of studying the reproducible nature and scan rate dependence of the hysteresis loop and high-temperature SCO with sufficient thermal stability has recently been pointed out in order to define the limiting characteristics of SCO materials [33,35–39].

Recently, we have focused on SCO molecules with 1-R-1*H*-1,2,3-triazole-containing Schiff-base (1-R-1*H*-1,2,3-triazolimine; R = Me and Ph) ligands since the ligand system can easily modify its structure with the choice of a substituent R of a precursor, 1-R-1*H*-1,2,3-triazole-4-carbaldehyde, and another amino precursor by simple click reaction [40–42], Schiff-base reaction [43] and replacement of R using the method reported by L'abbé and coworkers [44,45]. The iron(II) complexes with multidentate 1-R-1*H*-1,2,3-triazolimine ligand show a variety of SCO properties such as gradual, abrupt, and two-step transition with (or without) hysteresis in a wide temperature range (around RT, below RT and above RT over ca. 100 °C) [34,46,47]. In one of these studies, we reported the SCO iron(II) dinuclear double helicate for the first time [34]. This compound, with the formula $[Fe^{II}_2(L2^{C2})_2](PF_6)_4 \cdot 5H_2O \cdot MeCN$, has two bis-tridentate type ligand strands ($L2^{C2}$) in which two 1,2,3-triazolimine moieties of the ligand strand are bridged by an ethylene chain (Scheme 1), and shows an anomalous two-step SCO with 11 K-wide hysteresis in a second step centered at 432 K, which is the highest hysteretic transition temperature in the dinuclear SCO system reported so far [26–29,33,48].

From the fascinating structure and function of the $[Fe^{II}_2(L2^{C2})_2]^{4+}$ system, our own interest in the system has increasingly concerned the effect of the bridging alkyl chain length. We report here the synthesis, thermal stability, and structure of the corresponding propylene-bridged iron(II) dinuclear double helicate complexes $[Fe^{II}_2(L2^{C3})_2](PF_6)_4 \cdot 1.5H_2O \cdot 1.5MeCN$ (**1·PF$_6$**) and $[Fe^{II}_2(L2^{C3})_2](AsF_6)_4 \cdot 3H_2O \cdot MeCN$ (**1·AsF$_6$**), where $L2^{C3}$ = 1,1′-[propane-1,3-diylbis(1*H*-1,2,3-triazole-1,4-diyl)]bis{*N*-[2-(pyridin-2-yl)ethyl]methanimine} (Scheme 1), and the high-temperature hysteretic SCO of **1·AsF$_6$**.

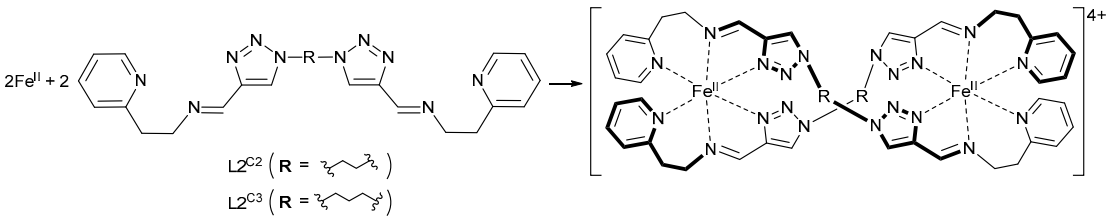

Scheme 1. Synthesis of the dinuclear double helicate complex-cation $[Fe^{II}_2(L2^{R})_2]^{4+}$ (R = C2 = ethylene [34], R = C3 = propylene (this work)).

2. Results and Discussion

*2.1. Synthesis and Characterization of $[Fe^{II}_2(L2^{C3})_2](PF_6)_4 \cdot 1.5H_2O \cdot 1.5MeCN$ (**1·PF$_6$**) and $[Fe^{II}_2(L2^{C3})_2](AsF_6)_4 \cdot 3H_2O \cdot MeCN$ (**1·AsF$_6$**)*

The ligand $L2^{C3}$ was prepared stoichiometric by the 1:2 condensation reaction of 1,1′-(propane-1,3-diyl)bis(1*H*-1,2,3-triazole-4-carbaldehyde) (**4**) and 2-(2-aminoethyl)pyridine. **4** was synthesized starting from 1-phenyl-1*H*-1,2,3-triazole-4-carbaldehyde and 1,3-diaminopropane (Scheme 2) based on the previously reported procedure of a related ethylene-bridged compound [34]. The dinuclear **1·PF$_6$** and **1·AsF$_6$** were prepared by mixing the ligand $L2^{C3}$, $Fe^{II}Cl_2 \cdot 4H_2O$, and KX (X = PF_6 and AsF_6 for **1·PF$_6$** and **1·AsF$_6$**, respectively) with a 1:1:2 molar ratio in MeOH/H_2O mixed solution, which was then recrystallized from the MeCN/MeOH mixed solution. All the synthetic procedures were performed in air and both complexes were obtained as dark-red block crystals. The infrared spectra of both showed a characteristic band at ca. 1609 cm^{-1}, corresponding to the C=N stretching vibration of the Schiff-base ligand [34,49]. In addition, characteristic bands at ca. 844 and 701 cm^{-1} were observed,

corresponding to the counter anions, PF_6^- and AsF_6^- for **1·PF$_6$** and **1·AsF$_6$**, respectively [34,49,50]. The formula of both complexes was confirmed by elemental analyses and thermogravimetric analyses. Thermogravimetry and differential thermal analysis (TG/DTA) curves of both are shown in Figure 1. As shown in Figure 1a, when the powdered sample of **1·PF$_6$** was heated from 30 °C (303 K) at a rate of 10 °C·min^{-1}, the sample weight decreased gradually and a weight loss of 4.3% at 224 °C (497 K) was observed, which corresponds to the calculated weight percentages of 0.5H_2O and 1.5MeCN molecules per $[Fe^{II}_2(L2^{C3})_2](PF_6)_4$·1.5$H_2O$·1.5MeCN (**1·PF$_6$**) (4.2%). Above this temperature, the weight loss became abrupt, and then the weight loss of the remaining one H_2O molecule (1.1%) was observed at 242 °C (515 K). In this region, a sharp thermal anomaly in DTA appeared (T_{max} = 232 °C (505 K)). Finally, above 242 °C (515 K), the weight loss became more and more abrupt, indicating the decomposition of **1·PF$_6$**. In the same way, as shown in Figure 1b, when the powdered sample of **1·AsF$_6$** was heated from 30 °C (303 K) at a rate of 10 °C·min^{-1}, the sample weight decreased gradually and the total weight loss was 5.0% at 215 °C (488 K) in agreement with the calculated weight percentage of 3H_2O and one MeCN molecule per $[Fe^{II}_2(L2^{C3})_2](AsF_6)_4$·3$H_2O$·MeCN (**1·AsF$_6$**) (5.1%). On further increasing the temperature from 215 °C (488 K), the desolvated sample of **1·AsF$_6$** was stable up to ca. 263 °C (536 K), and began to decompose above this temperature. Although a sharp thermal anomaly in DTA was also observed at T_{max} = 212 °C (485 K) in **1·AsF$_6$**, this peak was far from the decomposition temperature (ca. 263 °C), which is obviously different from that of **1·PF$_6$**. To access the reason for exhibiting a sharp thermal anomaly in DTA around 485–505 K, thermochromic properties of both compounds were also investigated (Figure 2). Although the orange-brown color of powdered samples of **1·PF$_6$** becomes slightly lighter from 300 K to ca. 483 K, possibly due to the partial SCO, further elevation of the temperature to 493 K induces rapid black coloration, suggesting the decomposition of the compound (Figure 2a). This thermochromic tendency and TG/DTA results suggest that the decomposition temperature overlaps the spin transition temperature in **1·PF$_6$**. On the other hand, powdered samples of **1·AsF$_6$** showed a clearly distinguishable thermochromism from orange-brown at 300 K to orange-yellow at ca. 498 K, suggesting the occurrence of SCO (Figure 2b). Then, further increasing the temperature to 503 K induces slight yellowish coloration, and ca. 5 min. later, a black coloration related to decomposition proceeds. This color change of **1·AsF$_6$** in a step-by-step-manner is comparable to the clear distinction between sharp thermal anomaly at T_{max} = 485 K and decomposition temperature observed in TG/DTA curves. Consequently, we decided to investigate SCO properties only for **1·AsF$_6$** which is more stable than **1·PF$_6$** in a high-temperature SCO region.

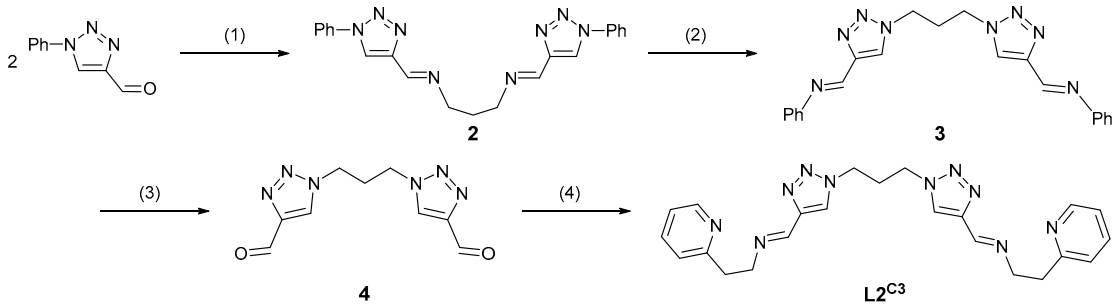

Scheme 2. Synthetic scheme of the ligand L2^{C2}. Reagents and conditions: (1) 1,3-diaminopropane, MeOH, 1 h, 60 °C; 78%; (2) 1-PrOH, 16 h, 80 °C; 78%; (3) HCl (aq), 2 h, room temperature (RT); 86%; (4) 2-(2-aminoethyl)pyridine (2 equiv), MeOH, 1 h, RT.

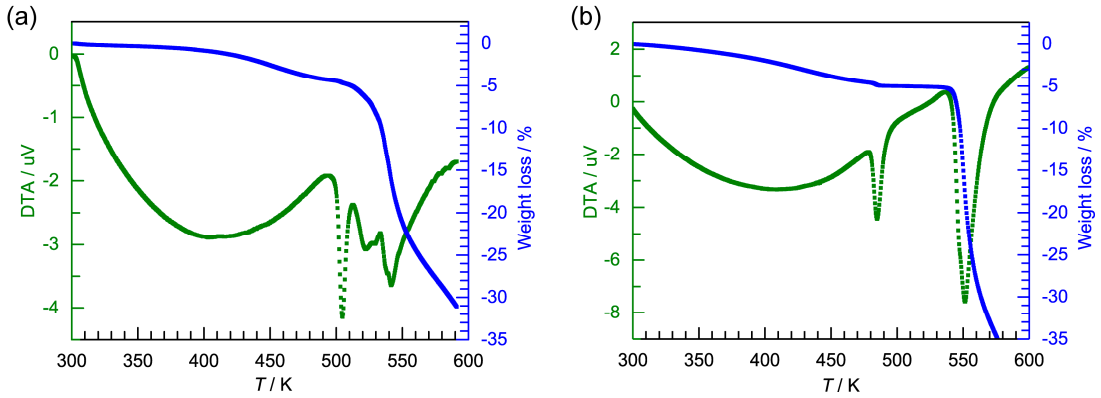

Figure 1. Thermogravimetry and differential thermal analysis (TG/DTA) curves of **1·PF$_6$** (**a**) and **1·AsF$_6$** (**b**).

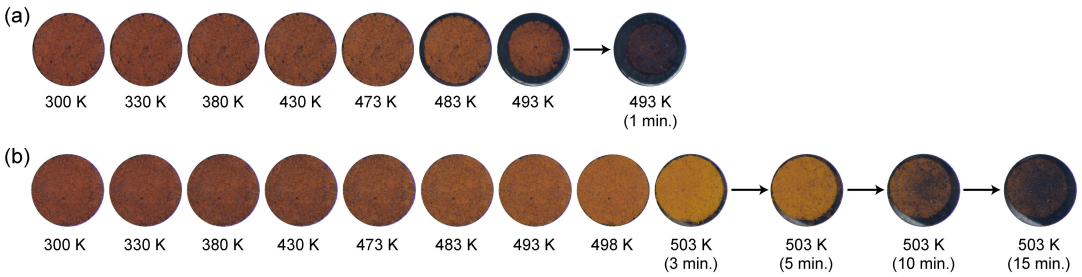

Figure 2. Temperature-dependent optical microscope images of grinding samples of **1·PF$_6$** (**a**) and **1·AsF$_6$** (**b**) deposited on a heating stage. Unless otherwise noted, after increasing the sample temperature at each target point, the sample was held for 5 min, and then an image was taken at each temperature.

2.2. Crystal Structure of 1·PF$_6$ and 1·AsF$_6$

The crystal structure of **1·PF$_6$** and **1·AsF$_6$** was determined at 120 K (low-spin–low-spin (LS–LS) state). As shown in Table 1, both complexes crystallize in the same monoclinic space group type *C*2/c (number 15) with $Z = 4$ and are isostructural. The structure consists of a $[Fe^{II}_2(L2^{C3})_2]^{4+}$ complex-cation, two disordered monovalent counterions (PF_6^- and AsF_6^- for **1·PF$_6$** and **1·AsF$_6$**, respectively), and H_2O and MeCN molecules as lattice solvents. In the crystal lattice, both solvent molecules are in the one solvent site in a severely disordered manner in both compounds. Thus, these regions, including solvent molecules, are treated with the *PLATON* SQUEEZE program [51] (see Experimental Section 3.3 including the details about analyses of disordered counter anions and solvent molecules).

Figure 3 shows the molecular structure of the complex-cation $[Fe^{II}_2(L2^{C3})_2]^{4+}$ of **1·AsF$_6$** at 120 K. As shown in Table 2, the structural feature of the complex-cation of **1·PF$_6$** is similar to that of **1·AsF$_6$**. Thus, we only discuss the structure of **1·AsF$_6$** below. The complex-cation has a dinuclear double-helical architecture, in which each ligand $L2^{C3}$ bound as a bis-tridentate ligand to two different iron centers, and conversely, the Fe^{II} centers are N6-coordinated pseudo-octahedral coordination environments bound to two different ligand strands. The intra-helical metal–metal distance is 10.894(3) Å, which is much longer than that of the related ethylene-bridged helicate $[Fe^{II}_2(L2^{C2})_2]^{4+}$ (7.855(3) Å) [34] due to the elongation of the alkyl chain from two to three C atoms. Each metal site is chiral, with either a Δ or a Λ configuration, and the complex-cation depicted in Figure 3 has a homochiral Λ–Λ pair. In the crystal, complex-cations with the Δ–Δ and Λ–Λ pairs coexist to form a racemic crystal since the complex crystallizes in a centrosymmetric space group, *C*2/c. The Fe–N coordination bond distances (1.954(3)–2.007(3) and 1.945(3)–2.007(3) Å for Fe1–N and Fe2–N, respectively) indicate that both centers are in the LS Fe^{II} state. While the average Fe–N bond distance and octahedral volume of

LS–LS $[Fe^{II}_2(L2^{C3})_2]^{4+}$ are similar to those of LS–LS $[Fe^{II}_2(L2^{C2})_2]^{4+}$, the Θ [52] and continuous shape measures (CShMs) relative to the regular octahedron with the center as the reference shape [53] of LS–LS $[Fe^{II}_2(L2^{C3})_2]^{4+}$ are lower than those of LS–LS $[Fe^{II}_2(L2^{C2})_2]^{4+}$, indicating that the Fe^{II} centers of LS–LS $[Fe^{II}_2(L2^{C3})_2]^{4+}$ have a more regular octahedral geometry than those of LS–LS $[Fe^{II}_2(L2^{C2})_2]^{4+}$ with the one minor exception of the Σ [54] of LS–LS $[Fe^{II}_2(L2^{C2})_2]^{4+}$, which is slightly lower than that of LS–LS $[Fe^{II}_2(L2^{C3})_2]^{4+}$ (average Fe–N bond distance, Σ, Θ, CShMs and octahedral volume of the LS–LS $[Fe^{II}_2(L2^{C2})_2]^{4+}$ for $[Fe^{II}_2(L2^{C2})_2](PF_6)_4{\cdot}5H_2O{\cdot}MeCN$ [34] are 1.971 Å, 42.5°, 133.7°, 0.696 and 10.096 $Å^3$, respectively).

Table 1. X-ray crystallographic data for **1·PF$_6$** and **1·AsF$_6$** at 120 K.

	$[Fe^{II}_2L2^{C3}_2](PF_6)_4$ 1.5H_2O·1.5MeCN (**1·PF$_6$**) [a]	$[Fe^{II}_2L2^{C3}_2](AsF_6)_4{\cdot}3H_2O{\cdot}MeCN$ (**1·AsF$_6$**) [a]
Formula	$C_{49}H_{59.5}N_{21.5}O_{1.5}P_4F_{24}Fe_2$	$C_{48}H_{61}N_{21}O_3As_4F_{24}Fe_2$
Formula weight	1665.26	1847.55
Crystal system	monoclinic	monoclinic
Space group	*C*2/*c* (No. 15)	*C*2/*c* (No.15)
a/Å	19.049(6)	19.410(3)
b/Å	19.056(5)	19.034(3)
c/Å	20.600(9)	20.772(5)
β/deg.	115.832(3)	115.723(2)
V/$Å^3$	6731(4)	6914(2)
Z	4	4
$d_{calcd.}$/g·cm^{-3}	1.643	1.775
μ (Mo Kα)/mm^{-1}	0.649	2.441
R_1 [b] (*I* > 2sigma(*I*))	0.0879	0.0520
wR_2 [c] (*I* > 2sigma(*I*))	0.2141	0.1167
R_1 [b] (all data)	0.1054	0.0626
wR_2 [c] (all data)	0.2286	0.1236
u [c]	0.0791	0.0425
v [c]	27.4133	16.3374
S	1.142	1.112
CCDC number	1544125	1544126

[a] The *PLATON* SQUEEZE program [51] was used to treat regions with highly disordered solvent molecules which could not be sensibly modeled in terms of atomic sites; [b] $R_1 = \Sigma||Fo| - |Fc||/\Sigma|Fo|$; [c] $wR_2 = [\Sigma w(|Fo|^2 - |Fc|^2)^2/\Sigma w|Fo^2|^2]^{1/2}$, $w = 1/[\sigma^2(|Fo|^2) + (uP)^2 + vP]$ where $P = (|Fo|^2 + 2|Fc|^2)/3$.

The assembly structure of **1·AsF$_6$** is shown in Figure 4. As shown in Figure 4a, a cationic one-dimensional (1D) structure is formed along the *b*-axis by slightly inclined intermolecular π–π interactions between all pyridyl rings of neighboring complex-cations with Cg1···Cg2 [ii] = 4.123(3) Å.

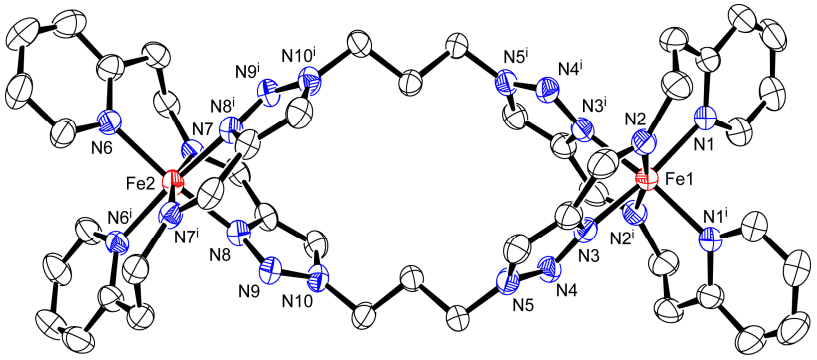

Figure 3. ORTEP drawing of the dinuclear double helicate complex-cation $[Fe^{II}_2(L2^{C3})_2]^{4+}$ of **1·AsF$_6$** at 120 K with the atom numbering scheme except for carbon atoms, where the thermal ellipsoids are drawn with a 50% probability level. H atoms have been omitted for clarity. Symmetry operation: (i) –x, y, 3/2 − z.

(Cg1 = centroid of the N1–C1–C2–C3–C4–C5 ring, Cg2 = centroid of the N6–C12–C13–C14–C15–C16 ring; symmetry operation: (ii) x, −1 + y, z; Table 3). In the light of chiral assembly, homochiral complex-cations are linked together in the π–stacked 1D structure to give a homochiral 1D chain (Δ–Δ···Δ–Δ···Δ–Δ··· or Λ–Λ···Λ–Λ···Λ–Λ···). Figure 4b shows the stacking observed between adjacent cationic 1D chains viewed along the *ac* plane. One-dimensional chains of opposite chirality are alternately arrayed along the *c*-axis to give a heterochiral crystal. Each cationic 1D chain is separated by AsF_6^- ions and solvent molecules occupying the space between the 1D chains in a strongly disordered manner even at 120 K. Although the assembly structure of **1·PF$_6$** is almost same as that of **1·AsF$_6$**, these 1D-based structures are remarkably different from the two-dimensional (2D) assembly of the related ethylene-bridged helicate $[Fe^{II}_2(L2^{C2})_2](PF_6)_4 \cdot 5H_2O \cdot MeCN$ by intermolecular π–π and CH/π interactions [34].

Table 2. Coordination bond lengths, angles, and structural parameters for **1·PF$_6$** and **1·AsF$_6$** at 120 K. CShMs: continuous shape measures.

Fe1 Site	1·PF$_6$	1·AsF$_6$	Fe2 Site	1·PF$_6$	1·AsF$_6$
Fe1–N Bond Lengths (Å)			Fe2–N Bond Lengths (Å)		
Fe1–N1	1.998(4)	2.007(3)	Fe2–N6	2.033(4)	2.007(3)
Fe1–N2	1.990(4)	1.970(4)	Fe2–N7	1.911(4)	1.962(3)
Fe1–N3	1.931(4)	1.954(3)	Fe2–N8	1.957(4)	1.945(3)
Fe1–N1 [i]	1.998(4)	2.007(3)	Fe2–N6 [i]	2.034(4)	2.007(3)
Fe1–N2 [i]	1.990(5)	1.970(4)	Fe2–N7 [i]	1.911(4)	1.962(3)
Fe1–N3 [i]	1.931(4)	1.954(3)	Fe2–N8 [i]	1.957(4)	1.945(3)
Average Fe1–N	1.973	1.977	Average Fe2–N	1.967	1.971
N–Fe1–N Bond Angles (°)			N–Fe2–N Bond Angles (°)		
N1–Fe1–N2	89.1(2)	91.35(15)	N6–Fe2–N7	93.38(17)	92.63(12)
N1–Fe1–N3	171.26(19)	170.93(14)	N6–Fe2–N8	172.89(15)	172.40(12)
N1–Fe1–N1 [i]	91.4(2)	92.67(18)	N6–Fe2–N6 [i]	93.9(2)	92.05(17)
N1–Fe1–N2 [i]	98.00(19)	95.70(14)	N6–Fe2–N7 [i]	95.50(16)	96.18(12)
N1–Fe1–N3 [i]	92.58(16)	91.47(12)	N6–Fe2–N8 [i]	89.72(17)	91.84(12)
N2–Fe1–N3	82.65(18)	80.20(13)	N7–Fe2–N8	80.17(17)	80.47(12)
N2–Fe1–N1 [i]	98.00(19)	95.69(15)	N7–Fe2–N6 [i]	95.50(16)	96.17(12)
N2–Fe1–N2 [i]	169.9(3)	169.79(18)	N7–Fe2–N7 [i]	167.0(3)	167.32(16)
N2–Fe1–N3 [i]	89.86(17)	92.27(13)	N7–Fe2–N8 [i]	90.38(16)	90.16(12)
N3–Fe1–N1 [i]	92.58(16)	91.47(12)	N8–Fe2–N6 [i]	89.72(17)	91.84(12)
N3–Fe1–N2 [i]	89.85(17)	92.27(13)	N8–Fe2–N7 [i]	90.38(16)	90.16(12)
N3-Fe1–N3 [i]	84.6(2)	85.61(17)	N8–Fe2–N8 [i]	87.3(3)	85.07(17)
N1 [i]–Fe1–N2 [i]	89.1(2)	91.36(15)	N6 [i]–Fe2–N7 [i]	93.38(17)	92.63(12)
N1 [i]–Fe1–N3 [i]	171.26(19)	170.93(14)	N6 [i]–Fe2–N8 [i]	172.89(15)	172.41(12)
N2 [i]–Fe1–N3 [i]	82.65(18)	80.20(14)	N7 [i]–Fe2–N8 [i]	80.17(17)	80.47(12)
Σ (°) [54]	44.8	48.2		45.3	47.7
Θ (°) [52]	113.9	120.1		106.9	108.1
CShMs [c] [53]	0.594	0.616		0.636	0.590
Octahedral volume (Å^3)	10.132	10.183		10.029	10.098

Symmetry operation: (i) −x, y, 3/2 – z; [c] The reference shape is the regular octahedron with center.

Table 3. Intermolecular contacts (Å) of π–π interaction for **1·PF$_6$** and **1·AsF$_6$** at 120 K.

	1·PF$_6$	1·AsF$_6$
Cg1 [a]···Cg2 [b,ii]	4.139(4)	4.123(3)
C3···C14 [ii]	3.582(13)	3.610(9)
C3···C15 [ii]	3.403(12)	3.423(8)
C4···C14 [ii]	3.432(11)	3.421(7)
C4···C15 [ii]	3.711(11)	3.703(6)

[a] Cg1 = centroid of the N1–C1–C2–C3–C4–C5 ring; [b] Cg2 = centroid of the N6–C12–C13–C14–C15–C16 ring. Symmetry operation: (ii) x, 1 + y, z for **1·PF$_6$** and x, −1 + y, z for **1·AsF$_6$**.

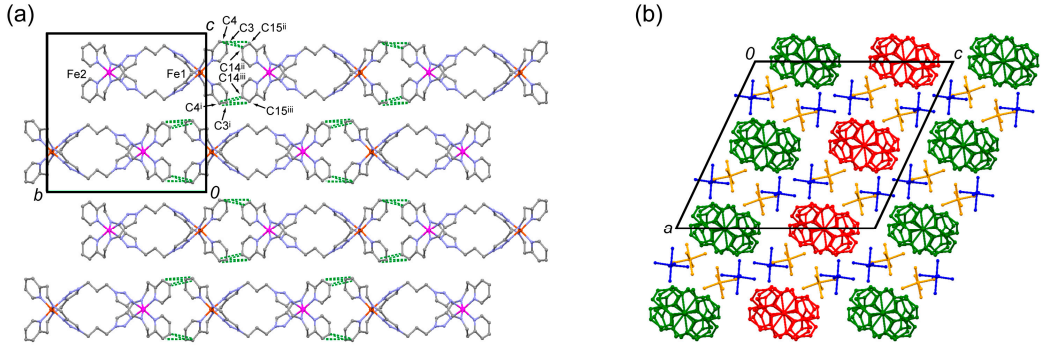

Figure 4. (**a**) Intermolecular interactions of **1·AsF$_6$** at 120 K. Adjacent complex-cations $[Fe^{II}{}_2(L2^{C3})_2]^{4+}$ with the same chirality are connected by intermolecular π–π interactions (green dotted line) to form the homochiral 1D chain structure along the *b*-axis. Symmetry operations: (i) −x, y, 3/2 − z; (ii) x, −1 + y, z; (iii) −x, −1 + y, 3/2 − z; (**b**) Packing diagram of **1·AsF$_6$** at 120 K viewed along the *ac* plane. Δ–Δ-$[Fe^{II}{}_2(L2^{C3})_2]^{4+}$ and Λ–Λ-$[Fe^{II}{}_2(L2^{C3})_2]^{4+}$ enantiomers are represented by green and red colors, respectively. Cationic 1D chains with the opposite chirality running along the *b*-axis exist in a crystal lattice to give a heterochiral crystal. Each cationic chain is separated by the space-occupying two disordered AsF_6^- ions (blue and orange; only the major component is indicated) and solvent molecules such as $3H_2O$ and one MeCN molecule (not indicated), which could not be sensibly modeled due to the strong disorder and regions including these solvent molecules being treated with the *PLATON* SQUEEZE program. H atoms have been omitted for clarity.

2.3. Magnetic Property of *1·AsF$_6$*

The magnetic susceptibilities for polycrystalline samples of **1·AsF$_6$** were measured upon heating from 300 to 498 K and subsequent cooling to 300 K at a sweep rate of 0.5 K·min^{-1} under an applied magnetic field of 1 T using a superconducting quantum interference device (SQUID) magnetometer with a special heating setup. The $\chi_M T$ vs. T plots are shown in Figure 5, where χ_M is the molar magnetic susceptibility per Fe and T is the absolute temperature. As shown in Figure 5, **1·AsF$_6$** showed an unsymmetrical hysteretic SCO above room temperature. The initial $\chi_M T$ value is 0.3 cm^3·K·mol^{-1} at 300 K, which is consistent with the theoretical value for a LS–LS Fe^{II} system. On raising the temperature from 300 K, the $\chi_M T$ value increases gradually to reach ca. 2.1 cm^3·K·mol^{-1} at 478 K, and then increases abruptly to reach ca. 6.3 cm^3·K·mol^{-1} at 498 K, which is consistent with the theoretical value for a high-spin–high-spin (HS–HS) Fe^{II} system ($\chi_M T$ = 6.0 cm^3·K·mol^{-1}). On lowering the temperature from 498 K, the $\chi_M T$ value decreases gradually, reaching ca. 4.3 cm^3·K·mol^{-1} at 409 K, and then decreases abruptly to reach ca. 1.5·cm^3·K mol^{-1} at 379 K. Then, the $\chi_M T$ value further decreases gradually to reach ca. 0.5 cm^3·K·mol^{-1} at 300 K. The critical temperatures of the warming ($T_c\uparrow$) and cooling ($T_c\downarrow$) modes in the abrupt spin transition area are 485 and 401 K, respectively, indicating the occurrence of ΔT = 84 K, which is the widest thermal hysteresis loop in the dinuclear system reported so far [26–29,33,34,48]. It is also noteworthy that the $T_c\uparrow$ of **1·AsF$_6$** is considerably higher than that of the related ethylene-bridged helicate $[Fe^{II}{}_2(L2^{C2})_2](PF_6)_4·5H_2O·MeCN$ ($T_c\uparrow$ = 437 K) [34] by about 48 K.

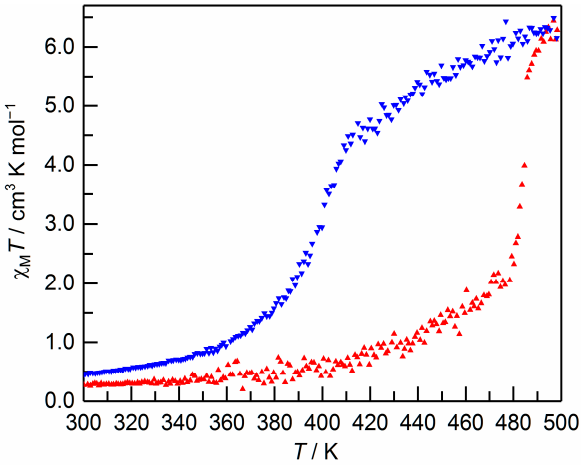

Figure 5. The magnetic behavior of **1·AsF$_6$** in the form of the $\chi_M T$ vs. T plots. **1·AsF$_6$** was warmed from 300 to 498 K (filled triangles; red), and then cooled from 498 to 300 K (filled inverted triangles; blue) at a sweep rate of 0.5 K·min^{-1}.

*2.4. Reproducibility of Hysteretic SCO of **1·AsF$_6$***

To reveal the desolvation effect and reproducibility of hysteretic SCO of **1·AsF$_6$**, temperature-dependent magnetic susceptibilities were also measured over three consecutive cycles. As shown in Figure 6a, although **1·AsF$_6$** shows a more gradual spin transition in the second cycle than in the first cycle, probably due to the in situ solvent liberation in the first heating, an asymmetric wide hysteresis loop is then still observed. Further thermal cycling (third cycle) causes the spin transition pattern to have a much more gradual and partial SCO fashion, which does not occur in the related ethylene-bridged helicate [Fe$^{II}_2$(L2^{C2})$_2$](PF$_6$)$_4$·5H$_2$O·MeCN [34]. Comparing powder X-ray diffraction (PXRD) patterns of as-synthesized **1·AsF$_6$** and after first thermal cycle of SQUID measurement confirms that there is no structural phase transition associated with the desolvation, because the peak patterns of the sample are not changed, although the peak positions increase slightly possibly due to the removal of solvent molecules and concomitant lattice contraction (Figure 6b). However, an intensity decrease and peak broadening are observed after three thermal cycles of SQUID measurement, presumably due to a loss of crystallinity and/or partial decomposition.

These properties were also confirmed by differential scanning calorimetry (DSC) experiments of four consecutive thermal cycles at a sweep rate of 10 K·min^{-1}, in the temperature range of 222–502 K (Figure 7). As shown in Figure 7, from the first cycle in heating and following cooling modes, a thermal hysteresis of ca. 85 K was detected ($T_{max}\uparrow$ and $T_{max}\downarrow$ are 498 and 413 K, respectively) and the hysteresis width is consistent with the ΔT value observed by the magnetic measurement. As the thermal cycling is repeated, the shape of DSC peaks becomes broader and smaller, and the position of the peak shifts to a lower temperature in both the heating and cooling modes of the second cycle due to the solvent loss in the first heating ($T_{max}\uparrow$ and $T_{max}\downarrow$ are 487 and 401 K, respectively, in the second cycle). However, further thermal cycling from the second cycle induces the peak shift to the opposite directions, in which the temperature variation in cooling modes is larger than that in heating modes ($T_{max}\uparrow$ and $T_{max}\downarrow$ are 490 and 392 K, respectively, in the third cycle, and 492 and 384 K, respectively, in the fourth cycle). In addition, peak broadening and reduction also continue in the third and fourth cycles. As a whole, thermal hysteresis of **1·AsF$_6$** is retained for at least four cycles, although the spin transition becomes gradual and incomplete with shifting the transition temperature due to the solvent liberation in the first cycle and a loss of crystallinity and/or partial decomposition upon further thermal cycling.

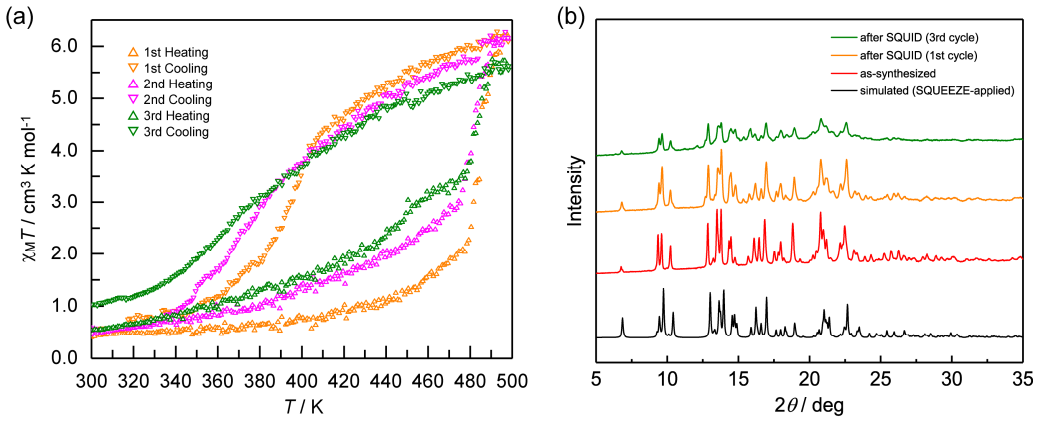

Figure 6. (**a**) Temperature dependence of the $\chi_M T$ product of **1·AsF$_6$** in the heating (empty triangles) and cooling (empty inverted triangles) modes over three successive thermal cycles at a sweep rate of 0.5 K·min^{-1}. Orange: first cycle; magenta: second cycle; olive: third cycle; (**b**) Powder X-ray diffraction (PXRD) patterns of **1·AsF$_6$** at RT in different states. Black: simulated from the SQUEEZE-applied single crystal X-ray data at 120 K; red: as-synthesized **1·AsF$_6$**; orange: **1·AsF$_6$** after the first thermal cycle of superconducting quantum interference device (SQUID) measurement; olive: **1·AsF$_6$** after a third thermal cycle of SQUID measurement.

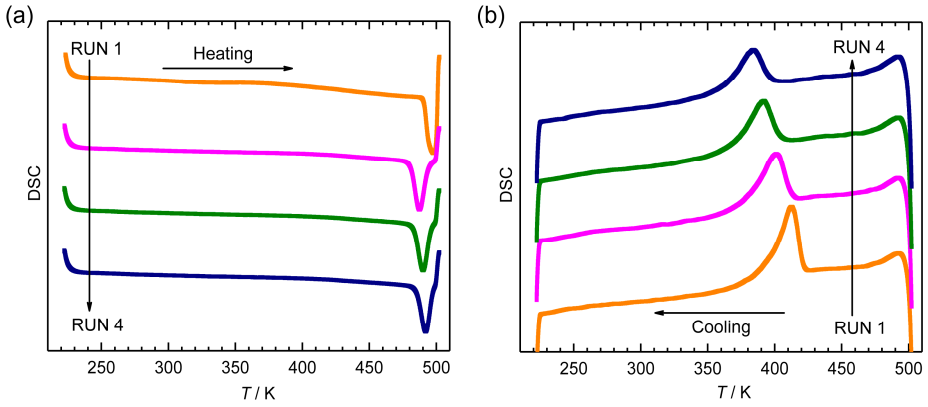

Figure 7. Differential scanning calorimetry (DSC) curves of **1·AsF$_6$** in the heating mode (**a**) and cooling mode (**b**) recorded over four successive thermal cycles at a sweep rate of 10 K·min^{-1}, in the temperature range of 222–502 K. Orange: first cycle; magenta: second cycle; olive: third cycle; navy blue: fourth cycle.

3. Materials and Methods

3.1. Synthesis of Fe^{II} Complexes

3.1.1. General

All reagents and solvents were purchased from commercial sources and used for the syntheses without further purification. The 1-Phenyl-1*H*-1,2,3-triazole-4-carbaldehyde was prepared according to methods in the literature [47]. The synthetic procedure of 1,1′-(propane-1,3-diyl)bis(1*H*-1,2,3-triazole-4-carbaldehyde) (**4**) was constructed by modifying the reported procedures [34]. All the synthetic procedures were carried out in air.

3.1.2. Preparation of 1,1′-(propane-1,3-diyl)bis(1*H*-1,2,3-triazole-4-carbaldehyde) (**4**)

To a warm pale yellow solution of 1-phenyl-1*H*-1,2,3-triazole-4-carbaldehyde (3.464 g, 20 mmol) in MeOH (30 mL), 1,3-diaminopropane (0.741 g, 10 mmol) in MeOH (1 mL) was added. The resulting

solution was stirred for 1 h at 60 °C, and was then cooled in a fridge. The precipitated white powders were collected by suction filtration, washed with Et_2O (10 mL × 3), and dried in vacuo. White solid of *N*,*N*′-(propane-1,3-diyl)bis[1-(1-phenyl-1*H*-1,2,3-triazol-4-yl)methanimine] (**2**). Yield: 3.005 g (78%). Mp 127–128 °C (from MeOH), ^{1}H NMR (600 MHz; DMSO-d6; TMS): δ 9.24 (s, 2H), 8.55 (s, 2H), 8.00–7.98 (m, 4H), 7.63–7.60 (m, 4H), 7.53–7.51 (m, 2H), 3.72 (t, *J* = 6.5 Hz, 4H), 2.05–2.00 (m, 2H). Anal. Calcd. for **2**·0.2H_2O = $C_{21}H_{20.4}N_8O_{0.2}$: C, 65.00; H, 5.30; N, 28.88%. Found: C, 65.05; H, 5.19; N, 29.01%.

A suspension of **2** (2.898 g, 7.5 mmol) in 1-PrOH (25 mL) was heated at 80 °C for 16 h, turning into a pale yellow solution, and the resulting solution was then cooled in a fridge. The precipitated white powders were collected by suction filtration, washed with Et_2O (10 mL), and dried in vacuo. White solid of 1,1′-[propane-1,3-diylbis(1*H*-1,2,3-triazole-1,4-diyl)]bis(*N*-phenylmethanimine) (**3**). Yield: 2.260 g (78%). m.p. 192–193 °C (from 1-PrOH), ^{1}H NMR (600 MHz; DMSO-d6; TMS): δ 8.78 (s, 2H), 8.67 (s, 2H), 7.43–7.41 (m, 4H), 7.28–7.25 (m, 6H), 4.52 (t, *J* = 6.9 Hz, 4H), 2.59–2.55 (m, 2H). Anal. Calcd. for **3**·0.35H_2O = $C_{21}H_{20.7}N_8O_{0.35}$: C, 64.55; H, 5.34; N, 28.68%. Found: C, 64.15; H, 5.20; N, 29.06%.

Hydrochloric acid (36%) (1.671 g, 16.5 mmol) in H_2O (28 mL) was added to white powders of **3** (2.125 g, 5.5 mmol), and the mixture was stirred for 2 h at room temperature. After turning the mixture into a yellowish-white suspension, the residual white solids of **4** were collected by suction filtration, washed with H_2O (10 mL) and then Et_2O (10 mL), and dried in vacuo. Yield: 1.103 g (86%). m.p. 124–125 °C (from H_2O), ^{1}H NMR (600 MHz; DMSO-d6; TMS): δ 10.03 (s, 2H), 8.89 (s, 2H), 4.52 (t, *J* = 6.9 Hz, 4H), 2.55–2.51 (m, 2H). Anal. Calcd. for $C_9H_{10}N_6O_2$: C, 46.15; H, 4.30; N, 35.88%. Found: C, 45.87; H, 4.19; N, 35.56%.

3.1.3. Synthesis of the Bis-Tridentate Ligand $L2^{C3}$ = 1,1′-[propane-1,3-diylbis(1*H*-1,2,3-triazole-1,4-diyl)]bis{*N*-[2-(pyridin-2-yl)ethyl]methanimine}

The ligand $L2^{C3}$ was prepared by mixing **4** and 2-(2-aminoethyl)pyridine with 1:2 molar ratio in MeOH. The ligand solution thus prepared was used for the synthesis of Fe^{II} complexes without further purification and isolation.

3.1.4. Preparation of $[Fe^{II}_2(L2^{C3})_2](PF_6)_4$·1.5$H_2O$·1.5MeCN (**1·PF$_6$**)

2-(2-Aminoethyl)pyridine (0.122 g, 1 mmol) in MeOH (1 mL) was added to a solution of **4** (0.118 g, 0.5 mmol) in MeOH (20 mL), and the resulting mixture was stirred at ambient temperature for 1 h. A pale yellow solution of the ligand (0.5 mmol) thus prepared was treated first with a solution of $Fe^{II}Cl_2$·4H_2O (0.099 g, 0.5 mmol) in MeOH (1 mL), turning into a dark orange-red solution, and then with KPF_6 (0.184 g, 1 mmol) in 4 mL of a mixed solution of MeOH and H_2O (1/1 by volume). The resulting mixture was stirred at ambient temperature for 1 h, during which time the precipitated orange-brown crude product was collected by suction filtration. The collected precipitate was dissolved in MeCN (4 mL) and then filtered. Dark-red block crystals were obtained by slow diffusion of MeOH (8 mL) into the filtrate (liquid–liquid diffusion) for a day. Yield: 0.154 g (37%). Anal. Calcd. for $[Fe^{II}_2(L2^{C3})_2](PF_6)_4$·1.5MeCN·1.5MeOH = $C_{49}H_{59.5}N_{21.5}O_{1.5}P_4F_{24}Fe_2$: C, 35.34; H, 3.60; N, 18.08%. Found: C, 35.48; H, 3.37; N, 18.06%. IR (KBr): $\nu_{C=N}$ 1609 cm^{-1}, ν_{P-F}(PF_6^-) 844 cm^{-1}.

3.1.5. Preparation of $[Fe^{II}_2(L2^{C3})_2](AsF_6)_4$·3$H_2O$·MeCN (**1·AsF$_6$**)

2-(2-Aminoethyl)pyridine (0.122 g, 1 mmol) in MeOH (2 mL) was added to a solution of **4** (0.118 g, 0.5 mmol) in MeOH (20 mL), and the resulting mixture was stirred at ambient temperature for 1 h. A pale yellow solution of the ligand (0.5 mmol) thus prepared was treated first with a solution of $Fe^{II}Cl_2$·4H_2O (0.099 g, 0.5 mmol) in MeOH (2 mL), turning into a dark orange-red solution, and then with $KAsF_6$ (0.228 g, 1 mmol) in 4 mL of a mixed solution of MeOH and H_2O (1/1 by volume). The resulting mixture was stirred at ambient temperature for 30 min, during which time the precipitated red-orange crude product was collected by suction filtration. The collected precipitate was dissolved in MeCN (3 mL) and then filtered. Dark-red block crystals were obtained by slow diffusion of MeOH (7 mL) into the filtrate (liquid–liquid diffusion) for a day. Yield: 0.155 g (33%). Anal. Calcd. for

$[Fe^{II}_2(L2^{C3})_2](AsF_6)_4 \cdot 3H_2O \cdot MeCN = C_{48}H_{61}N_{21}O_3As_4F_{24}Fe_2$: C, 31.21; H, 3.33; N, 15.92%. Found: C, 31.46; H, 3.04; N, 16.25%. IR (KBr): $\nu_{C=N}$ 1609 cm^{-1}, $\nu_{As-F}(AsF_6^-)$ 701 cm^{-1}.

3.2. Physical Measurements

Elemental C, H, and N analyses were performed on a J-Science Lab (Kyoto, Japan) MICRO CORDER JM-10. IR spectra were recorded at room temperature using a JASCO (Tokyo, Japan) FT/IR 460Plus spectrophotometer or a PerkinElmer (Waltham, MA, USA) Spectrum100 FT-IR spectrometer with the samples prepared as KBr disks. ^{1}H NMR spectra were recorded on a JEOL (Tokyo, Japan) ECA-600 spectrometer. The melting point was measured through a Yanaco (Kyoto, Japan) MP-S3 micro melting point meter and was uncorrected. Thermogravimetric data were collected on a TG/DTA6300 (SII Nano Technology Inc., Chiba, Japan) instrument in the temperature range of 30–318 °C (303–591 K) for **1·PF$_6$** and 30–381 °C (303–654 K) for **1·AsF$_6$** at a rate of 10 K·min^{-1} under a nitrogen atmosphere. DSC measurements for **1·AsF$_6$** were performed with a DSC6200 (SII Nano Technology Inc., Chiba, Japan) over the temperature range of 222–502 K, at a sweep rate of 10 K·min^{-1} under a nitrogen atmosphere using aluminum hermetic pans with an empty pan as reference. Magnetic susceptibilities of **1·AsF$_6$** were measured in the temperature range of 300–498 K at a sweep rate of 0.5 K·min^{-1} under an applied magnetic field of 1 T using a Quantum Design (San Diego, CA, USA) MPMS-7 SQUID magnetometer with a special heating setup of a sample space oven option. The sample was wrapped in an aluminum foil and was then inserted into a quartz glass tube with a small amount of glass wool filler. Corrections for diamagnetism of the sample were made using Pascal's constants [55] and a background correction for the sample holder was applied. PXRD patterns were recorded at room temperature on a portion of polycrystalline powders placed on a non-reflecting silicon plate, using a Rigaku (Tokyo, Japan) MiniFlex600 diffractometer with Cu Kα radiation (λ = 1.5418 Å) operated at 0.4 kW power (40 kV, 10 mA). Images of grinding samples were recorded under an optical microscope SMZ800N (Nikon, Tokyo, Japan). The sample temperature was controlled by using a Linkam (Tadworth, UK) THMS 600 heating and freezing stage.

3.3. Crystallographic Data Collection and Structure Analyses

X-ray diffraction data of **1·PF$_6$** and **1·AsF$_6$** were collected by a Rigaku (Tokyo, Japan) AFC7R Mercury CCD diffractometer using graphite monochromated Mo Kα radiation (λ = 0.71075 Å) operated at 5 kW power (50 kV, 100 mA). A single crystal was mounted on a MiTeGen (Ithaca, NY, USA) MicroMount (200 μm) with liquid paraffin, then rapidly frozen in a nitrogen-gas stream at 120 K to avoid the loss of crystal solvents and the diffraction data were collected at 120 K. The temperature of the crystal was maintained by means of a Rigaku cooling device to within an accuracy of ±2 K. The data were corrected for Lorentz, polarization, and absorption effects. The structures were solved by the direct method [56] and refined on F^2 data using the full-matrix least-squares algorithm using *SHELXL*-2014 [57]. Non-hydrogen atoms were refined anisotropically. The structure of **1·PF$_6$** contains two disordered PF_6^- ions. Both PF_6^- ions were disordered over two positions and the occupancy factors for the possible two positions of F atoms (F1A–F6A:F1B–F6B = 0.518(15):0.482(15) for P(1)F_6^- and F7A–F12A:F7B–F12B = 0.635(16):0.365(16) for P(2)F_6^-) were refined using the tools available from the *SHELXL*-2014 program package. In the refinement of these disordered PF_6^- ions, the SADI command for all P–F bonds and F···F distances and the RIGU command for all P and F atoms were also applied. In addition, diffraction quality of the crystal of **1·PF$_6$** was not sufficient to model highly disordered solvent molecules. The *PLATON* SQUEEZE program (290617, A.L. Spek, Utrecht, NL-UT, The Netherlands) [51] was used to treat regions with disordered solvent molecules which could not be sensibly modelled in terms of atomic sites. Available void volume was 892 Å^3. Then, 196 electrons per unit cell were located and these were assigned to 1.5 H_2O and 1.5 MeCN molecules per complex (196/4 = 49 e per complex; 1.5 H_2O (15) + 1.5 MeCN (33) = 48 electrons). In the same way, the structure of **1·AsF$_6$** contains two disordered AsF_6^- ions and severely disordered solvent molecules. In **1·AsF$_6$**, both AsF_6^- ions were disordered over three positions and the occupancy factors for the possible

three positions of F atoms (F1A–F6A:F1B–F6B:F1C–F6C = 0.434(3):0.291(3):0.275(3) for As(1)F_6^- and F7A–F12A:F7B–F12B:F7C–F12C = 0.513(3):0.219(3):0.268(3) for As(2)F_6^-) were refined using the SUMP command to keep the sum of three occupancy factors of each ion as 1.0. In the refinement of these disordered AsF_6^- ions, the SADI command for all As–F bonds and F···F distances, the RIGU command for all As and F atoms, and the EADP command for F5A, F5B, F5C and F6A, F6B, F6C were also applied. The *PLATON* SQUEEZE program was also used to treat regions with disordered solvent molecules in the structure of **1·AsF$_6$**. Available void volume was 926 Å^3, and 220 electrons per unit cell were located. These were assigned to 3 H_2O and 1 MeCN molecules per complex (220/4 = 55 e per complex; 3 H_2O (30) + 1 MeCN (22) = 52 electrons). All H atoms were placed in geometrically calculated positions, with the distances of C–H = 0.95 (aromatic) and 0.99 (CH_2) Å, and refined as riding atoms, with *U*iso(H) = 1.2 *U*eq(C). All calculations were performed by using the Yadokari-XG software package [58]. The CShMs of the Fe^{II} centers relative to the ideal octahedron were calculated by SHAPE 2.1 [53]. The octahedral volumes of the Fe^{II} centers were calculated by *OLEX2* [59]. CCDC 1544125–1544126 contains the supplementary crystallographic data for this paper. These data can be obtained free of charge via http://www.ccdc.cam.ac.uk/conts/retrieving.html or from the CCDC (12 Union Road, Cambridge CB2 1EZ, UK; Fax: +44 1223 336033; E-mail: deposit@ccdc.cam.ac.uk).

4. Conclusions

In conclusion, the present work reveals the effects of the extension of the bridging alkyl chain length (from C2 to C3) on the structure and SCO properties of the iron(II) dinuclear double helicate $[Fe^{II}_2(L2^R)_2](X)_4$·solvent, with the concomitant effects of the coexistent counter anions and lattice solvents. While propylene-bridged dinuclear complexes $[Fe^{II}_2(L2^{C3})_2](PF_6)_4·1.5H_2O·1.5MeCN$ (**1·PF$_6$**) and $[Fe^{II}_2(L2^{C3})_2](AsF_6)_4·3H_2O·MeCN$ (**1·AsF$_6$**) are isostructural, the thermal stability of **1·PF$_6$** is lower than that of **1·AsF$_6$** in a high-temperature SCO region. **1·AsF$_6$** shows an unsymmetrical hysteretic SCO between the LS–LS and HS–HS states at above room temperature with ΔT = 84 K ($T_c\uparrow$ = 485 K and $T_c\downarrow$ = 401 K in the abrupt spin transition area) in the first thermal cycle, which is the widest hysteresis loop in the dinuclear system reported so far. In addition, the $T_c\uparrow$ of **1·AsF$_6$** is considerably higher than that of the related ethylene-bridged compound, by about 48 K. This high-temperature wide thermal hysteresis may be related to the 1D assembly structure composed of inter-helicate π–π interactions, which is obviously different from the 2D assembly of the related ethylene-bridged compound. Although the desolvation of **1·AsF$_6$** does not directly affect the assembly structure, consecutive thermal cycles cause a loss of crystallinity and/or partial decomposition, and subsequent modification of the hysteretic SCO loop to a more gradual and partial fashion. As a consequence, the extension of the bridging alkyl chain length (from C2 to C3) and subsequent elongation of the dinuclear cation makes the 2D supramolecular assembly one-dimensional, and enhances the width of the hysteresis loop. Simultaneous raising of the $T_c\uparrow$ may also cause the overlapping between spin transition temperature and decomposition temperature, which is related to the thermal durability upon SCO.

Supplementary Materials: The following are available online at www.mdpi.com/2304-6740/5/3/49/s1. Cif and cif-checked files.

Acknowledgments: This work was partly funded by the Gifu University for the promotion of the research of young scientists. Part of this work was conducted at the Institute for Molecular Science, supported by the Nanotechnology Platform Program (Molecule and Material Synthesis) of the Ministry of Education, Culture, Sports, Science and Technology (MEXT), Japan. The authors would like to thank Professor O. Sakurada (Gifu University, Japan) for his assistance in collecting PXRD data.

Author Contributions: The experimental work was performed mainly by Shiori Hora with assistance from Hiroaki Hagiwara. Hiroaki Hagiwara supervised the experiments. Both authors analyzed the data and contributed to the preparation of the manuscript.

Conflicts of Interest: The authors declare no conflict of interest.

References

1. Gütlich, P.; Goodwin, H.A. (Eds.) *Spin Crossover in Transition Metal Compounds I-III*; Topics in Current Chemistry; Springer: Berlin, Germany, 2004; Volume 233–235.
2. Halcrow, M.A. (Ed.) *Spin-Crossover Materials–Properties and Applications*; John Wiley & Sons: Chichester, UK, 2013.
3. Gütlich, P.; Gaspar, A.B.; Garcia, Y. Spin state switching in iron coordination compounds. *Beilstein J. Org. Chem.* **2013**, *9*, 342–391. [CrossRef] [PubMed]
4. Jenkins, D.M.; Peters, J.C. Solution and Solid-State Spin-Crossover Behavior in a Pseudotetrahedral d^7 Ion. *J. Am. Chem. Soc.* **2003**, *125*, 11162–11163. [CrossRef] [PubMed]
5. Li, J.; Lord, R.L.; Noll, B.C.; Baik, M.-H.; Schulz, C.E.; Scheidt, W.R. Cyanide: A Strong-Field Ligand for Ferrohemes and Hemoproteins? *Angew. Chem. Int. Ed.* **2008**, *47*, 10144–10146.
6. Scepaniak, J.J.; Harris, T.D.; Vogel, C.S.; Sutter, J.; Meyer, K.; Smith, J.M. Spin Crossover in a Four-Coordinate Iron(II) Complex. *J. Am. Chem. Soc.* **2011**, *133*, 3824–3827. [PubMed]
7. Mossin, S.; Tran, B.L.; Adhikari, D.; Pink, M.; Heinemann, F.W.; Sutter, J.; Szilagyi, R.K.; Meyer, K.; Mindiola, D.J. A Mononuclear Fe(III) Single Molecule Magnet with a 3/2↔5/2 Spin Crossover. *J. Am. Chem. Soc.* **2012**, *134*, 13651–13661. [PubMed]
8. Weber, B.; Bauer, W.; Obel, J. An Iron(II) Spin-Crossover Complex with a 70 K Wide Thermal Hysteresis Loop. *Angew. Chem. Int. Ed.* **2008**, *47*, 10098–10101. [CrossRef] [PubMed]
9. Weber, B.; Bauer, W.; Pfaffender, T.; Dîrtu, M.M.; Naik, A.D.; Rotaru, A.; Garcia, Y. Influence of Hydrogen Bonding on the Hysteresis Width in Iron(II) Spin-Crossover Complexes. *Eur. J. Inorg. Chem.* **2011**, *2011*, 3193–3206.
10. Zhao, X.-H.; Zhang, S.-L.; Shao, D.; Wang, X.-Y. Spin Crossover in $[Fe(2\text{-Picolylamine})_3]^{2+}$ Adjusted by Organosulfonate Anions. *Inorg. Chem.* **2015**, *54*, 7857–7867. [CrossRef] [PubMed]
11. Hayami, S.; Gu, Z.-Z.; Yoshiki, H.; Fujishima, A.; Sato, O. Iron (III) spin-crossover compounds with a wide apparent thermal hysteresis around room temperature. *J. Am. Chem. Soc.* **2001**, *123*, 11644–11650. [PubMed]
12. Schäfer, B.; Rajnák, C.; Šalitroš, I.; Fuhr, O.; Klar, D.; Schmitz-Antoniak, C.; Weschke, E.; Wende, H.; Ruben, M. Room temperature switching of a neutral molecular iron(II) complex. *Chem. Commun.* **2013**, *49*, 10986–10988. [CrossRef] [PubMed]
13. Iasco, O.; Rivière, E.; Guillot, R.; Cointe, M.B.-L.; Meunier, J.-F.; Bousseksou, A.; Boillot, M.-L. $Fe^{II}(pap\text{-}5NO_2)_2$ and $Fe^{II}(qsal\text{-}5NO_2)_2$ Schiff-Base Spin-Crossover Complexes: A Rare Example with Photomagnetism and Room-Temperature Bistability. *Inorg. Chem.* **2015**, *54*, 1791–1799. [CrossRef] [PubMed]
14. Kröber, J.; Codjovi, E.; Kahn, O.; Grolière, F.; Jay, C. A Spin Transition System with a Thermal Hysteresis at Room Temperature. *J. Am. Chem. Soc.* **1993**, *115*, 9810–9811. [CrossRef]
15. Kahn, O.; Martinez, C.J. Spin-Transition Polymers: From Molecular Materials toward Memory Devices. *Science* **1998**, *279*, 44–48. [CrossRef]
16. Muñoz-Lara, F.J.; Gaspar, A.B.; Aravena, D.; Ruiz, D.; Muñoz, M.C.; Ohba, M.; Ohtani, R.; Kitagawa, S.; Real, J.A. Enhanced bistability by guest inclusion in Fe(II) spin crossover porous coordination polymers. *Chem. Commun.* **2012**, *48*, 4686–4688. [CrossRef] [PubMed]
17. Lochenie, C.; Bauer, W.; Railliet, A.P.; Schlamp, S.; Garcia, Y.; Weber, B. Large Thermal Hysteresis for Iron(II) Spin Crossover Complexes with *N*-(Pyrid-4-yl)isonicotinamide. *Inorg. Chem.* **2014**, *53*, 11563–11572. [CrossRef] [PubMed]
18. Dîrtu, M.M.; Naik, A.D.; Rotaru, A.; Spinu, L.; Poelman, D.; Garcia, Y. Fe^{II} Spin Transition Materials Including an Amino–Ester 1,2,4-Triazole Derivative, Operating at, below, and above Room Temperature. *Inorg. Chem.* **2016**, *55*, 4278–4295. [CrossRef] [PubMed]
19. Murray, K.S. Advances in Polynuclear Iron(II), Iron(III) and Cobalt(II) Spin-Crossover Compounds. *Eur. J. Inorg. Chem.* **2008**, 3101–3121. [CrossRef]
20. Nihei, M.; Sekine, Y.; Suganami, N.; Nakazawa, K.; Nakao, A.; Nakao, H.; Murakami, Y.; Oshio, H. Controlled Intramolecular Electron Transfers in Cyanide-Bridged Molecular Squares by Chemical Modifications and External Stimuli. *J. Am. Chem. Soc.* **2011**, *133*, 3592–3600. [CrossRef] [PubMed]
21. Hietsoi, O.; Dunk, P.W.; Stout, H.D.; Arroyave, A.; Kovnir, K.; Irons, R.E.; Kassenova, N.; Erkasov, R.; Achim, C.; Shatruk, M. Spin Crossover in Tetranuclear Fe(II) Complexes, $\{[(tpma)Fe(\mu\text{-}CN)]_4\}X_4$ (X = ClO_4^-, BF_4^-). *Inorg. Chem.* **2014**, *53*, 13070–13077. [CrossRef] [PubMed]

22. Matsumoto, T.; Newton, G.N.; Shiga, T.; Hayami, S.; Matsui, Y.; Okamoto, H.; Kumai, R.; Murakami, Y.; Oshio, H. Programmable spin-state switching in a mixed-valence spin-crossover iron grid. *Nat. Commun.* **2014**, *5*, 3865. [CrossRef] [PubMed]
23. Wu, S.-Q.; Wang, Y.-T.; Cui, A.-L.; Kou, H.-Z. Toward Higher Nuclearity: Tetranuclear Cobalt(II) Metallogrid Exhibiting Spin Crossover. *Inorg. Chem.* **2014**, *53*, 2613–2618. [CrossRef] [PubMed]
24. Steinert, M.; Schneider, B.; Dechert, S.; Demeshko, S.; Meyer, F. Spin-State Versatility in a Series of Fe_4 [2 × 2] Grid Complexes: Effects of Counteranions, Lattice Solvent, and Intramolecular Cooperativity. *Inorg. Chem.* **2016**, *55*, 2363–2373. [CrossRef] [PubMed]
25. Charbonnière, L.J.; Williams, A.F.; Piguet, C.; Bernardinelli, G.; Rivara-Minten, E. Structural, Magnetic, and Electrochemical Properties of Dinuclear Triple Helices: Comparison with Their Mononuclear Analogues. *Chem. Eur. J.* **1998**, *4*, 485–493. [CrossRef]
26. Ksenofontov, V.; Gaspar, A.B.; Niel, V.; Reiman, S.; Real, J.A.; Gütlich, P. On the Nature of the Plateau in Two-Step Dinuclear Spin-Crossover Complexes. *Chem. Eur. J.* **2004**, *10*, 1291–1298. [CrossRef] [PubMed]
27. Weber, B.; Kaps, E.S.; Obel, J.; Achterhold, K.; Parak, F.G. Synthesis and Characterization of a Dinuclear Iron(II) Spin Crossover Complex with Wide Hysteresis. *Inorg. Chem.* **2008**, *47*, 10779–10787. [CrossRef] [PubMed]
28. Min, K.S.; Swierczek, K.; DiPasquale, A.G.; Rheingold, A.L.; Reiff, W.M.; Arif, A.M.; Miller, J.S. A dinuclear iron(II) complex, $[(TPyA)Fe^{II}(THBQ^{2-})Fe^{II}(TPyA)](BF_4)_2$ [TPyA = tris(2-pyridylmethyl)amine; $THBQ^{2-}$ = 2,3,5,6-tetrahydroxy-1,4-benzoquinonate] exhibiting both spin crossover with hysteresis and ferromagnetic exchange. *Chem. Commun.* **2008**, 317–319. [CrossRef]
29. Sunatsuki, Y.; Kawamoto, R.; Fujita, K.; Maruyama, H.; Suzuki, T.; Ishida, H.; Kojima, M.; Iijima, S.; Matsumoto, N. Structures and Spin States of Bis(tridentate)-Type Mononuclear and Triple Helicate Dinuclear Iron(II) Complexes of Imidazole-4-carbaldehyde azine. *Inorg. Chem.* **2009**, *48*, 8784–8795. [CrossRef] [PubMed]
30. Sunatsuki, Y.; Kawamoto, R.; Fujita, K.; Maruyama, H.; Suzuki, T.; Ishida, H.; Kojima, M.; Iijima, S.; Matsumoto, N. Structures and spin states of mono- and dinuclear iron(II) complexes of imidazole-4-carbaldehyde azine and its derivatives. *Coord. Chem. Rev.* **2010**, *254*, 1871–1881. [CrossRef]
31. Archer, R.J.; Hawes, C.S.; Jameson, G.N.L.; Mckee, V.; Moubaraki, B.; Chilton, N.F.; Murray, K.S.; Schmitt, W.; Kruger, P.E. Partial spin crossover behaviour in a dinuclear iron(II) triple helicate. *Dalton Trans.* **2011**, *40*, 12368–12373. [CrossRef] [PubMed]
32. Schneider, C.J.; Cashion, J.D.; Chilton, N.F.; Etrillard, C.; Fuentealba, M.; Howard, J.A.K.; Létard, J.-F.; Milsmann, C.; Moubaraki, B.; Sparkes, H.A.; et al. Spin Crossover in a 3,5-Bis(2-pyridyl)-1,2,4-triazolate-Bridged Dinuclear Iron(II) Complex $[\{Fe(NCBH3)(py)\}_2\text{-}(\mu\text{-}L^1)_2]$—Powder versus Single Crystal Study. *Eur. J. Inorg. Chem.* **2013**, *2013*, 850–864. [CrossRef]
33. Kulmaczewski, R.; Olguín, J.; Kitchen, J.A.; Feltham, H.L.C.; Jameson, G.N.L.; Tallon, J.L.; Brooker, S. Remarkable Scan Rate Dependence for a Highly Constrained Dinuclear Iron(II) Spin Crossover Complex with a Wide Thermal Hysteresis Loop. *J. Am. Chem. Soc.* **2014**, *136*, 878–881. [CrossRef] [PubMed]
34. Hagiwara, H.; Tanaka, T.; Hora, S. Synthesis, structure, and spin crossover above room temperature of a mononuclear and related dinuclear double helicate iron(II) complexes. *Dalton Trans.* **2016**, *45*, 17132–17140. [CrossRef] [PubMed]
35. Halcrow, M.A. Spin-crossover Compounds with Wide Thermal Hysteresis. *Chem. Lett.* **2014**, *43*, 1178–1188. [CrossRef]
36. Brooker, S. Spin crossover with thermal hysteresis: Practicalities and lessons learnt. *Chem. Soc. Rev.* **2015**, *44*, 2880–2892. [CrossRef] [PubMed]
37. Fujinami, T.; Nishi, K.; Hamada, D.; Murakami, K.; Matsumoto, N.; Iijima, S.; Kojima, M.; Sunatsuki, Y. Scan Rate Dependent Spin Crossover Iron(II) Complex with Two Different Relaxations and Thermal Hysteresis *fac*-$[Fe^{II}(HL^{n\text{-}Pr})_3]Cl{\cdot}PF_6$ ($HL^{n\text{-}Pr}$ = 2-Methylimidazol-4-yl-methylideneamino-*n*-propyl). *Inorg. Chem.* **2015**, *54*, 7291–7300. [CrossRef] [PubMed]
38. Bao, X.; Guo, P.-H.; Liu, W.; Tucek, J.; Zhang, W.-X.; Leng, J.-D.; Chen, X.-M.; Gural'skiy, I.; Salmon, L.; Bousseksou, A.; et al. Remarkably high-temperature spin transition exhibited by new 2D metal–organic frameworks. *Chem. Sci.* **2012**, *3*, 1629–1633. [CrossRef]
39. Liu, W.; Bao, X.; Li, J.-Y.; Qin, Y.-L.; Chen, Y.-C.; Ni, Z.-P.; Tong, M.-L. High-Temperature Spin Crossover in Two Solvent-Free Coordination Polymers with Unusual High Thermal Stability. *Inorg. Chem.* **2015**, *54*, 3006–3011. [CrossRef] [PubMed]

40. Rostovtsev, V.V.; Green, L.G.; Fokin, V.V.; Sharpless, K.B. A Stepwise Huisgen Cycloaddition Process: Copper(I)-Catalyzed Regioselective "Ligation" of Azides and Terminal Alkynes. *Angew. Chem. Int. Ed.* **2002**, *41*, 2596–2599. [CrossRef]
41. Tornøe, C.W.; Christensen, C.; Meldal, M. Peptidotriazoles on Solid Phase: [1,2,3]-Triazoles by Regiospecific Copper(I)-Catalyzed 1,3-Dipolar Cycloadditions of Terminal Alkynes to Azides. *J. Org. Chem.* **2002**, *67*, 3057–3064. [CrossRef] [PubMed]
42. Pathigoolla, A.; Pola, R.P.; Sureshan, K.M. A versatile solvent-free azide–alkyne click reaction catalyzed by in situ generated copper nanoparticles. *Appl. Catal. A: Gen.* **2013**, *453*, 151–158. [CrossRef]
43. Schiff, H. Mittheilungen aus dem Universitätslaboratorium in Pisa: Eine neue Reihe organischer Basen. *Justus Liebigs Ann. Chem.* **1864**, *131*, 118–119. [CrossRef]
44. L'abbé, G.; Bruynseels, M. Replacement of aryl by alkyl in 1-substituted 1H-1,2,3-triazole-4-carbaldehydes. *J. Chem. Soc. Perkin Trans. 1* **1990**, 1492–1493. [CrossRef]
45. L'abbé, G.; Bruynseels, M.; Delbeke, P.; Toppet, S. Molecular rearrangements of 4-iminomethyl-1,2,3-triazoles. Replacement of 1-aryl substituents in 1H-1,2,3-triazole-4-carbaldehydes. *J. Heterocycl. Chem.* **1990**, *27*, 2021–2027. [CrossRef]
46. Hagiwara, H.; Minoura, R.; Okada, S.; Sunatsuki, Y. Synthesis, Structure, and Magnetic Property of a New Mononuclear Iron (II) Spin Crossover Complex with a Tripodal Ligand Containing Three 1, 2, 3-Triazole Groups. *Chem. Lett.* **2014**, *43*, 950–952. [CrossRef]
47. Hagiwara, H.; Okada, S. A polymorphism-dependent $T_{1/2}$ shift of 100 K in a hysteretic spin-crossover complex related to differences in intermolecular weak CH···X hydrogen bonds (X = S vs. S and N). *Chem. Commun.* **2016**, *52*, 815–818. [CrossRef] [PubMed]
48. Schneider, C.J.; Moubaraki, B.; Cashion, J.D.; Turner, D.R.; Leita, B.A.; Batten, S.R.; Murray, K.S. Spin crossover in di-, tri- and tetranuclear, mixed-ligand tris(pyrazolyl)methane iron(II) complexes. *Dalton Trans.* **2011**, *40*, 6939–6951. [CrossRef] [PubMed]
49. Nakamoto, K. *Infrared and Raman Spectra of Inorganic and Coordination Compounds*, 6th ed.; John Wiley & Sons: Hoboken, NJ, USA, 2009.
50. Yamada, M.; Hagiwara, H.; Torigoe, H.; Matsumoto, N.; Kojima, M.; Dahan, F.; Tuchagues, J.-P.; Re, N.; Iijima, S. A Variety of Spin-Crossover Behaviors Depending on the Counter Anion: Two-Dimensional Complexes Constructed by NH···Cl^- Hydrogen Bonds, $[Fe^{II}H_3L^{Me}]Cl{\cdot}X$ (X = PF_6^-, AsF_6^-, SbF_6^-, $CF_3SO_3^-$; H_3L^{Me} = Tris[2-{[(2-methylimidazol-4-yl)methylidene]amino}ethyl]amine). *Chem. Eur. J.* **2006**, *12*, 4536–4549. [CrossRef] [PubMed]
51. Spek, A.L. *PLATON* SQUEEZE: A tool for the calculation of the disordered solvent contribution to the calculated structure factors. *Acta Crystallogr. Sect. C Struct. Chem.* **2015**, *71*, 9–18. [CrossRef] [PubMed]
52. Marchivie, M.; Guionneau, P.; Létard, J.-F.; Chasseau, D. Photo-induced spin-transition: The role of the iron(II) environment distortion. *Acta Crystallogr. Sect. B* **2005**, *61*, 25–28. [CrossRef] [PubMed]
53. Llunell, M.; Casanova, D.; Cirera, J.; Alemany, P.; Alvarez, S. *SHAPE2.1. Program for Calculating Continuous Shape Measures of Polyhedral Structures*; Universitat de Barcelona: Barcelona, Spain, 2013.
54. Guionneau, P.; Marchivie, M.; Bravic, G.; Létard, J.-F.; Chasseau, D. Structural aspects of spin crossover. Examples of the $[Fe^{II}L_n(NCS)_2]$ complexes. *Top. Curr. Chem.* **2004**, *234*, 97–128.
55. Kahn, O. *Molecular Magnetism*; VCH: Weinheim, Germany, 1993.
56. Burla, M.C.; Caliandro, R.; Carrozzini, B.; Cascarano, G.L.; Cuocci, C.; Giacovazzo, C.; Mallamo, M.; Mazzone, A.; Polidori, G. Crystal structure determination and refinement via *SIR2014*. *J. Appl. Cryst.* **2015**, *48*, 306–309. [CrossRef]
57. Sheldrick, G.M. Crystal structure refinement with *SHELXL*. *Acta Cryst.* **2015**, *C71*, 3–8.
58. Kabuto, C.; Akine, S.; Nemoto, T.; Kwon, E. Release of Software (Yadokari-XG 2009) for Crystal Structure Analyses. *J. Cryst. Soc. Jpn.* **2009**, *51*, 218–224. [CrossRef]
59. Dolomanov, O.V.; Bourhis, L.J.; Gildea, R.J.; Howard, J.A.K.; Puschmann, H. *OLEX2*: A complete structure solution, refinement and analysis program. *J. Appl. Cryst.* **2009**, *42*, 339–341. [CrossRef]